JOURNAL OF GEOPHYSICAL RESEARCH, VOL. 100, NO. A8, PAGES 14,569–14,580, AUGUST 1, 1995

Ionospheric electron densities calculated using different EUV flux models and cross sections: Comparison with radar data

M. J. Buonsanto,[1] P. G. Richards,[2] W. K. Tobiska,[3] S. C. Solomon,[4] Y.-K. Tung,[1,5] and J. A. Fennelly[6]

Abstract. The recent availability of the new EUVAC (Richards et al., 1994) and EUV94X (Tobiska, 1993b, 1994) solar flux models and new wavelength bin averaged photoionization and photoabsorption cross section sets led us to investigate how these new flux models and cross sections compare with each other and how well electron densities (N_e) calculated using them compare with actual measurements collected by the incoherent scatter radar at Millstone Hill (42.6°N, 288.5°E). In this study we use the Millstone Hill semiempirical ionospheric model, which has been developed from the photochemical model of Buonsanto et al. (1992). For the $F2$ region, this model uses determinations of the motion term in the N_e continuity equation obtained from nine-position radar data. We also include two simulations from the field line interhemispheric plasma (FLIP) model. All the model results underestimate the measured N_e in the E region, except that the EUV94X model produces reasonable agreement with the data at the E region peak because of a large Lyman β (1026 Å) flux, but gives an unrealistically deep E-$F1$ valley. The ionospheric models predict that the O_2^+ density is larger than the NO^+ density in the E region, while numerous rocket measurements show a larger NO^+ density. Thus the discrepancy between the ionospheric models and the radar data in the E region is most likely due to an incomplete understanding of the NO^+ chemistry. In the $F2$ region, the photoionization rate given by EUV94X is significantly larger than that given by the EUVAC and earlier models. This is due to larger EUV fluxes in EUV94X compared to EUVAC over the entire 300–1050 Å wavelength range, apart from some individual spectral lines. In the case of EUVAC, this is partly compensated for by larger photoelectron impact ionization due to the larger EUV fluxes below 250 Å. The differences between ionospheric model results for the different cross-section sets are generally much smaller than the differences with the data.

1. Introduction

Modeling of ionospheric electron and ion densities requires knowledge of EUV and soft X-ray solar fluxes, photoelectron fluxes, photoionization and photoabsorption cross sections, chemical reaction rates for each species, and neutral composition. While the photochemistry of the $F2$ region is relatively simple compared to the E and $F1$ regions, modeling the $F2$ region also requires knowledge of neutral winds, electric fields and diffusion processes, which together give the motion term $\nabla\bullet(N_e\mathbf{v})$ in the electron density (N_e) continuity equation

$$\frac{\partial N_e}{\partial t} = q - \beta N_e - \nabla\bullet(N_e\mathbf{v}) \quad (1)$$

Here q is the production rate due to photoionization and secondary photoelectron impact, β is the recombination rate, and $\mathbf{v}$ is the plasma drift velocity.

In the past few years a photochemical model of the midlatitude E and $F1$ regions has been developed at Millstone Hill (42.6°N, 288.5°E) and results compared with incoherent scatter daytime observations taken at this location [*Buonsanto*, 1990; *Buonsanto et al.*, 1992]. This model has been improved and extended to the $F2$ region by including a more comprehensive minor ion chemistry, allowing diurnal variations, and combining the photochemical calculations with measurements of the motion term in the continuity equation obtained from a nine-position radar experiment. This yields a semiempirical model of the ionosphere above Millstone Hill which may be compared with radar data at a variety of heights and for a variety of conditions to give information about the accuracy of the model chemistry and inputs. A strength of this model is its flexibility, in that it is designed to be used with a variety of EUV flux models and cross-section sets. Recently, two new wavelength bin averaged EUV flux models have been published, the EUVAC model [*Richards et al.*, 1994] and the EUV94X model [*Tobiska*, 1993b, 1994]. Richards et al. have also published a new set of bin-averaged photoionization and photoabsorption cross sections, based on the detailed compilation of *Fennelly and Torr* [1992]. These new solar flux models and cross sections have been included as possible options for use by the updated Millstone Hill ionospheric model. The purpose of this paper is to investigate how these new solar flux models compare with each other, and how N_e calcu-

[1]Massachusetts Institute of Technology, Haystack Observatory, Westford.
[2]Computer Science Department and Center for Space Plasma and Aeronomic Research, University of Alabama, Huntsville.
[3]Telos/Jet Propulsion Laboratory, Pasadena, California.
[4]Laboratory for Atmospheric and Space Physics, University of Colorado, Boulder.
[5]Physics Department, University of California, Berkeley.
[6]Earth System Science Laboratory, University of Alabama, Huntsville.

Paper number 95JA00680.
0148-0227/95/95JA-00680$05.00

lated using them compares with N_e calculated using previous standard solar flux models and N_e observed with the incoherent scatter radar. We also compare results of the new *Richards et al.* [1994] cross-section sets with results from the older cross section sets. In addition to the Millstone Hill ionosphere model, we also use the field line interhemispheric plasma (FLIP) model, as described by *Torr et al.* [1990] for two simulations to see whether our conclusions are dependent on the choice of ionospheric model. For the *F*2 region, measurement of the motion term in the continuity equation permits us to compute the recombination rate β from (1), and compare it with β calculated using MSIS-86 [*Hedin*, 1987] neutral densities.

2. Ionosphere and Solar Flux Models

2.1. Semiempirical Model

As described above, the Millstone Hill semiempirical ionospheric model consists of two components, a calculated photochemistry, which is sufficient to model the *E* and *F*1 region electron and ion densities, and a measured term associated with ionospheric motions, which is needed in addition to the photochemistry to reproduce *F*2 region electron and ion densities. The neutral composition and temperature are taken from the MSIS-86 model. We do not attempt to model the ion and electron temperatures; these are taken from Millstone Hill data. By including as much empirical information as possible in the model, we hope to obtain more reliable information about the accuracy of the EUV and photoelectron flux models, cross sections, reaction rates, and MSIS-86 model inputs.

2.1.1. Photochemistry. The photochemistry used in the current work has been described in detail previously [*Buonsanto*, 1990; *Buonsanto et al.*, 1992], but a number of additional reactions have been added to improve the minor ion chemistry. Chemical rate coefficients for ion-neutral and ion recombination reactions now included in the model are listed in Table 1. We now use new rates for $O^+(^2P) + N_2$ and $O^+(^2P) + O$ reactions from *Chang et al.* [1993]. Additional improvements to the model are inclusion of photoionization of NO by solar Lyman alpha 1216Å giving NO^+, dissociative ionization of O_2 and N_2, and photoionization of atomic nitrogen.

For the attenuation of the solar fluxes, we have previously used an analytical approximation to the Chapman function for calculation of the optical depth [*Titheridge*, 1988]. We now prefer the more direct approach of integrating through the overlying atmosphere which is represented by the MSIS-86 model. For this purpose, *Rees* [1989] provides separate optical depth formulae for solar zenith angle χ less than or greater than 90°. Direct implementation of these formulae in a numerical model is difficult due to a singularity at χ=90°. Making a change of variable, we combine these two formulae to yield

$$\tau(\lambda, \chi_0, z_0) = \sum_j \sigma_j^a(\lambda)\,(R + z_0)\,\sin\chi_0 \int_0^{\chi_0} \frac{n_j(\chi)}{\sin^2\chi}\,d\chi \qquad (2)$$

Table 1. Reactions Included in the Revised Photochemical Model

Reaction	Rate Coefficient, $m^3\ s^{-1}$, or Rate, s^{-1}	Reference
$O^+(^4S) + N_2 \rightarrow NO^+ + N$	$k_1 = 1.533\times10^{-18} - 5.92\times10^{-19}(T_f/300) + 8.6\times10^{-20}(T_f/300)^2$ ($T_f < 1700$ K) $k_1 = 2.73\times10^{-18} - 1.155\times10^{-18}(T_f/300) + 1.483\times10^{-19}(T_f/300)^2$ ($T_f \geq 1200$ K)	*St. Maurice and Torr* [1978]
$O^+(^4S) + O_2 \rightarrow O_2^+ + O$	$k_2 = 1.25\times10^{-23}T_f^2 - 3.7\times10^{-20}T_f + 3.1\times10^{-17}$	*Torr et al.* [1988]
$O^+(^2D) + N_2 \rightarrow N_2^+ + O$	$k_3 = 8\times10^{-16}$	*Johnsen and Biondi* [1980]
$O^+(^2D) + O_2 \rightarrow O_2^+ + O$	$k_4 = 7\times10^{-16}$	*Johnsen and Biondi* [1980]
$O^+(^2D) + O \rightarrow O^+(^4S) + O$	$k_5 = 5\times10^{-18}$	*Abdou et al.* [1984]
$O^+(^2D) + e \rightarrow O^+(^4S) + e$	$k_6 = 6.6\times10^{-14}(300/T_e)^{0.5}$	*Henry et al.* [1969]
$O^+(^2P) + O \rightarrow O^+(^4S) + O$	$k_7 = 4.0\times10^{-16}$	*Chang et al.* [1993]
$O^+(^2P) + N_2 \rightarrow N_2^+ + O$	$k_8 = 3.4\times10^{-16}$	*Chang et al.* [1993]
$O^+(^2P) + O_2 \rightarrow O_2^+ + O$	$k_9 = 4.8\times10^{-16}$	*Link* [1982]
$O^+(^2P) + e \rightarrow O^+(^2D) + e$	$k_{10} = 1.5\times10^{-13}(300/T_e)^{0.5}$	*Henry et al.* [1969]
$O^+(^2P) + e \rightarrow O^+(^4S) + e$	$k_{11} = 4.0\times10^{-14}(300/T_e)^{0.5}$	*Henry et al.* [1969]
$O^+(^2P) \rightarrow O^+(^2D) + h\nu$	$A_1 = 0.172\ s^{-1}$	*Seaton and Osterbrock* [1957]
$O^+(^2P) \rightarrow O^+(^4S) + h\nu$	$A_2 = 0.047\ s^{-1}$	*Seaton and Osterbrock* [1957]
$N_2^+ + O \rightarrow O^+(^4S) + N_2$	$k_{12a} = 9.8\times10^{-18}(300/T_i)^{0.23}$	*McFarland et al.* [1974]
$N_2^+ + O \rightarrow NO^+ + N$	$k_{12b} = 1.4\times10^{-16}(300/T_i)^{0.44} - k_{12a}$	*McFarland et al.* [1974]
$N_2^+ + O_2 \rightarrow O_2^+ + N_2$	$k_{13} = 5\times10^{-17}(300/T)$	*Lindinger et al.* [1974]
$N_2^+ + e \rightarrow N + N$	$\alpha_3 = 2.7\times10^{-13}$	*Abdou et al.* [1984]
$O_2^+ + NO \rightarrow NO^+ + O_2$	$k_{14} = 4.5\times10^{-16}$	*Lindinger et al.* [1974]
$O_2^+ + N \rightarrow NO^+ + O$	$k_{15} = 1.2\times10^{-16}$	*Fehsenfeld* [1977]
$O_2^+ + e \rightarrow O + O$	$\alpha_2 = 2\times10^{-13}(300/T_e)^{0.7}$ ($T_e < 1200$ K) $\alpha_2 = 1.6\times10^{-13}(300/T_e)^{0.55}$ ($T_e \geq 1200$ K)	*Walls and Dunn* [1974] *Torr et al.* [1976]
$NO^+ + e \rightarrow N + O$	$\alpha_1 = 4.3\times10^{-13}(300/T_e)$	*Torr and Torr* [1979]
$N^+ + O_2 \rightarrow NO^+ + O$	$k_{16} = 2.6\times10^{-16}$	*Langford et al.* [1985]
$N^+ + O_2 \rightarrow O^+(^4S) + NO$	$k_{17} = 3\times10^{-17}$	*Rees* [1989]
$N^+ + O_2 \rightarrow O_2^+ + N$	$k_{18} = 3.1\times10^{-16}$	*Langford et al.* [1985]
$N^+ + O \rightarrow O^+(^4S) + N$	$k_{18} = 1\times10^{-18}$	*Torr* [1985]

where τ is the optical depth at wavelength λ, zenith angle χ_0, and height z_0, the summation j is over the three neutral species O, N_2, and O_2, the densities of which (n_j) are obtained from the MSIS-86 model, σ^a_j is the photoabsorption cross section for species j at wavelength λ, and R is the Earth's radius.

Nighttime sources of ionization have now been included, based on [*Strobel et al.*, 1974, 1980, J. E. Titheridge, personal communication, 1992]. The sources included are starlight, scattering of solar radiation off interplanetary H and He, and resonantly scattered airglow. In our simple parameterization, starlight contributes to the 900–1000Å continuum and at Lyman β (1026Å) and has a simple seasonal variation, the interplanetary background contributes at 584Å (He I) and at Lyman β and has a seasonal and solar cycle dependence, and airglow contributes at 304Å (He II), 584Å (He I), and Lyman β and has a zenith angle and solar cycle variation. Airglow is the dominant photoionization source closer to sunrise and sunset. Starlight and the interplanetary background make significant contributions closer to midnight, with starlight more important. Additional details are provided by *Tung* [1993]. While these nocturnal sources have little effect on the *F* region, they provide a source for the residual nighttime ionization in the *E* region.

The *pe/pi* ratio is the rate of ionization by secondary photoelectron impact divided by the photoionization rate. The model currently has three options for this. These are the formulation of *Lilensten et al.* [1989], the formulae by *Richards and Torr* [1988], or values directly read into the program from the global airglow (GLOW) model [*Solomon et al.*, 1988; *Solomon and Abreu*, 1989].

2.1.2. F2 region. For modeling the *F*2 region the photochemistry described above has to be combined with ionospheric motions induced by winds, electric fields, and diffusion. These motions give the motion term $\nabla\bullet(N_e\mathbf{v})$ in the continuity equation (1). In our semiempirical modeling approach, $\nabla\bullet(N_e\mathbf{v})$ is measured directly from nine-position incoherent scatter radar data above Millstone Hill, as described previously [*Buonsanto and Holt*, 1995]. In brief, analysis of data from nine positions allows us to estimate spatial gradients in the components of the ion drift vector $\mathbf{v}$ and in the ionospheric scalar parameters N_e, T_e, and T_i. The spatial gradients in components of $\mathbf{v}$ and in N_e allow estimation of $\nabla\bullet(N_e\mathbf{v})$. We can calculate N_e from

$$N_e = [q - \partial N_e/\partial t - \nabla\bullet(N_e\mathbf{v})]/\beta \quad (3)$$

where q and β are obtained from the photochemical calculations and the MSIS-86 neutral atmosphere model, and $\partial N_e/\partial t$, $\nabla\bullet(N\mathbf{v})$ are measured. The seven-value magnetic index array is input to MSIS-86 to specify the magnetic activity over the 59 hours prior to the current time [*Hedin*, 1987]. In practice, an equation of the form of (1) is solved for each ion species included in the model ($O^+(^4S)$, $O^+(^2D)$, $O^+(^2P)$, NO^+, O_2^+, N_2^+, and N^+), and the results combined.

Alternately, we estimate β for $O^+(^4S)$ from

$$\beta = [q - \partial N_e/\partial t - \nabla\bullet(N_e\mathbf{v})]/N_e \quad (4)$$

where q is the modeled production rate for $O^+(^4S)$, and $\partial N_e/\partial t$, $\nabla\bullet(N_e\mathbf{v})$, and N_e are the measured values multiplied by the fraction of ions which are $O^+(^4S)$ in the model (usually ≈ 98–100% in the *F*2 region). We compare the results of (4) with calculations of β using

$$\beta = k_1[N_2] + k_2[O_2] \quad (5)$$

where we use the measured ion temperature T_i, the MSIS-86 model for $[N_2]$, $[O_2]$, and neutral temperature T_n, and the rate coefficients k_1 and k_2 are given in Table 1.

2.2. EUV Flux Models

The measured solar spectrum is seldom available for aeronomical modeling purposes, so modelers rely on solar flux models, which are keyed to measurements of one or more solar spectral lines on the date to be modeled, or averaged over one or more solar rotations. The most commonly used proxy for the solar ionizing radiation is the widely available 10.7 cm flux, or *F*10.7. These models of the EUV and longer wavelength soft X-ray fluxes are usually bin-averaged into a convenient number of wavelength bands and important solar emission lines spanning the range of approximately 30Å (3 nm) up to 1050 Å (105 nm). These wavelengths originate in the sun's chromosphere, transition region, and corona, and are characterized by considerable variability and large solar cycle variations. It is beyond the scope of this paper to discuss in detail the development of the various EUV flux models, or the arguments for or against them. These have been reviewed by *Lean* [1990], *Tobiska* [1993a], and *Richards et al.* [1994]. Suffice it to say that there are significant differences between the models and their abilities to reproduce solar activity variations in EUV fluxes. Even when the overall solar activity variations are reproduced in some average sense, none of the models can be expected to be very accurate in reproducing the EUV fluxes on a particular day. As pointed out by *Hinteregger* [1981], this is due to the great variety of types of solar active regions and differences in their evolution over different time scales, so that EUV models based on some limited set of measurements over a limited time period could give quite misleading results if applied to a different part of the same solar cycle, or even worse, to a different solar cycle. We will restrict our discussion of the EUV flux models to brief descriptions of those which are compared in the current work.

Hinteregger et al. [1981] developed the first proxy model based on Atmospheric Explorer E (AE-E) data. An important contribution of this work was the development of the solar minimum reference spectrum called SC#21REFW. Hinteregger et al. described an EUV two-class (chromospheric and coronal) model which was extended beyond the time period of the AE-E mission by using a two variable (*F*10.7 and 81 day mean of *F*10.7) association formula. *Torr and Torr* [1985] published bin-averaged solar fluxes for 37 wavelength bands and significant EUV emission lines for the two AE-E reference spectra SC#21REFW and F79050N, the latter representing solar maximum. A common method for estimating the EUV fluxes in use by aeronomers has been to interpolate between these two bin-averaged spectra using *F*10.7. An inconsistency with measurements of the shape of the photoelectron flux spectrum [*Richards and Torr*, 1984], as well as an inconsistency with the broad band solar flux measurements of [*Ogawa and Judge*, 1986] suggests that the Hinteregger et al. model fluxes below 250 Å should be increased by a factor of 2 or more. However, *Richards et al.* [1994] have pointed out other problems with the Hinteregger model, including the SC#21REFW spectrum and the scaling with solar activity.

Richards et al. [1994] have introduced a new EUV flux model for aeronomic calculations (EUVAC), which is based on a measured solar minimum reference spectrum called F74113 [*Heroux and Hinteregger*, 1978, *Torr et al.*, 1979] and the relative solar activity variations of the [*Hinteregger et al.*, 1981] proxy model. EUVAC provides fluxes in the 37 wavelength bins of [*Torr et al.*, 1979; *Torr and Torr*, 1985], and the solar activity proxy is the mean of the daily

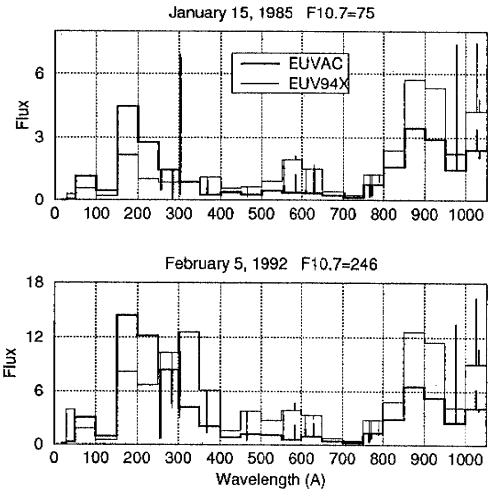

Figure 1. Bin-averaged solar fluxes (10^{13} photons m^{-2} s^{-1}) for 39 wavelength bins and discrete emission lines for the EUVAC (thick lines) and EUV94X (thin lines) solar flux models. (top) Solar minimum and (bottom) solar maximum.

$F10.7$ and the 81-day average $F10.7$. EUVAC model coefficients for two additional wavelength bands (18–30Å and 30–50Å) have been calculated for use in the present study.

W. K. Tobiska and coworkers have produced a series of solar flux models, the latest version of which is called EUV94X [*Tobiska*, 1993b, 1994]. This model provides solar fluxes in 39 wavelength bins from 18 to 1050 Å, the latter 37 bins corresponding to the bins of Torr et al. This model was constructed using a multiple linear regression technique, incorporating several satellite EUV data sets as well as results from several rocket experiments. Solar activity variations in the model are established using two chromospheric proxies, Lyman α and He I 10,830 Å equivalent width scaled to Lyman α, and two coronal proxies, $F10.7$ and the 81-day mean of $F10.7$. If either or both of the chromospheric proxies are not provided by the user, they are estimated in the model from the $F10.7$ and its 81-day mean.

Figure 1 shows a comparison between solar fluxes from the two most recent models (EUVAC and EUV94X) for 1 day near solar minimum, and for 1 day near solar maximum. For both dates, EUV fluxes are larger in EUV94X than in EUVAC over the entire 300–1050 Å range, apart from some individual spectral lines. Below 250 Å, EUVAC fluxes are larger on both dates, except at 30–50 Å. The large EUV94X flux at 30–50 Å is based on the originally published measurements by the SOLRAD 11 satellite. In the EUVAC model, the fluxes from the F74113 spectrum were increased by a factor of 2 between 150 and 250 Å, and increased by a factor of 3 below 150 Å to improve the agreement between calculated and measured photoelectron fluxes. This accounts for the large EUVAC fluxes below 250 Å. Although the larger EUV94X fluxes above 300 Å result in larger photoionization, the larger EUVAC fluxes in the 50–250 Å range produce larger ionization from secondary photoelectron impact which compensates somewhat for this.

2.3. Photoionization and Photoabsorption Cross-Section Models

In this paper we compare results obtained using three different wavelength-bin averaged photoionization and photoabsorption cross section sets.

The first set is based on the widely used cross sections published by *Torr et al.* [1979] in 37 wavelength bins from 50 to 1050 Å. The Torr et al. cross sections are intensity-weighted bin averages of the high resolution tabulations of *Kirby et al.* [1979]. The Millstone Hill model also requires cross sections from 18 to 50 Å, and we obtain the cross sections at these short wavelengths from the GLOW model. *Torr et al.* [1979] did not publish dissociative ionization cross sections for N_2 and O_2, so for these we have also used cross sections from the GLOW model. Similarly, Torr et al. did not publish photoionization cross sections for atomic nitrogen; for these we have used values from [*Fennelly and Torr*, 1992; *Richards et al.*, 1994].

The second set of cross sections used in this study is that from the GLOW model. The GLOW model cross sections are based on the compilation of *Conway* [1988]. These values differ from the earlier *Kirby et al.* [1979] compilation primarily in that the atomic oxygen ionization cross section is reduced at the shorter wavelengths, following the measurements of *Samson and Pareek* [1985]. The cross sections were averaged for each wavelength bin, weighted by the SC#21REFW solar minimum spectrum in that bin. There are no GLOW model photoionization cross sections for atomic nitrogen, so again we have used the values from [*Fennelly and Torr*, 1992; *Richards et al.*, 1994].

The third set of cross sections used in this work is that of [*Fennelly and Torr*, 1992], which have been bin-averaged into 37 wavelength bands between 50 and 1050Å by *Richards et al.* [1994]. The *Fennelly and Torr* [1992] compilation includes results of more recent measurements and includes the dense structure and autoionization structure in the photoabsorption and photoionization cross sections. The tables include, for the first time, cases where the photoionization and photoabsorption cross sections for atomic oxygen are not equal. Also this is the first compilation to include photoionization cross sections for atomic nitrogen. Recent results by *Bell and Stafford* [1992] for the photoionization cross sections for $O^+(^4P)$ and $O^+(^2P^*)$ are considerably different from the *Fennelly and Torr* [1992] values, which were based on *Kirby et al.* [1979]. For this third set of cross sections we have adjusted the $O^+(^4P)$ and $O^+(^2P^*)$ cross sections in line with *Bell and Stafford*'s [1992] results. This gives only a small difference in the final concentrations of $O^+(^4S)$ calculated by the model (< 2%).

2.4. Field Line Interhemispheric Plasma Model

The field line interhemispheric plasma (FLIP) model, which has been developed over a period of more than ten years, has been described previously by *Richards and Torr* [1988] and more recently by *Torr et al.* [1990]. The main component of this one-dimensional model calculates the plasma densities and temperatures along entire magnetic flux tubes from 80 km in the northern hemisphere through the plasmasphere to 80 km in the southern hemisphere. The model uses a tilted dipole approximation to the Earth's magnetic field. The equations solved are the continuity and momentum equations for O^+, H^+, and He^+, as formulated for the topside ionosphere by *St.-Maurice and Schunk* [1977]. Collisions between ions and neutrals have been included in order to extend the equations into the E and F regions. The electron and ion temperatures are obtained by solving the energy equations [*Schunk and Nagy*, 1978]. Electron heating due to photoelectrons is provided by a solution of the two-stream photoelectron flux equations using the method of *Nagy and Banks* [1970]. The solutions have been extended to encompass the entire field line on the same spatial grid as the ion continuity and momentum equations.

3. Incoherent Scatter Radar Data

The Millstone Hill E and $F1$ region (below 200 km) electron density profiles presented here were obtained using a short (40 μs) pulse with 6-km resolution. These profiles were calibrated using *foF2* from the local Digisonde, and temperature and Debye length corrections were applied using ion and electron temperature profiles constructed from the available longer pulse measurements at the greater heights and from the MSIS-86 model at the lower heights [*Buonsanto*, 1989, 1990]. For most of the profiles, representative error bars are calculated at 120 km and 150 km using the method outlined by *Evans* [1969]. Since it is extremely difficult to simultaneously fit incoherent scatter spectra in the E and $F1$ regions for temperature and ion composition, a standard ion composition profile is assumed in the reduction of Millstone Hill data, which assumes 50% O^+ at 180 km. As is done in earlier work [*Buonsanto*, 1990; *Buonsanto et al.*, 1992], we use ion composition profiles calculated by the Millstone Hill model, together with factors given by *Waldteufel* [1971], to correct the observed incoherent scatter N_e, T_e, and T_i measurements. The revised temperatures are then input to the model and a new profile calculated. This procedure is repeated iteratively until convergence to final temperature and ion composition profiles. Some of the N_e profiles displayed in this paper were previously shown [*Buonsanto et al.*, 1992], though with different model corrections. The use of these profiles allows us to see whether there are any significant differences between results of the updated model and those of the preceding version.

For the diurnal variations of the observed N_e at 180 km, and for the $F2$ region above Millstone Hill, we show results from fits to the 300 μs pulse-length data. The original data have 45 km height resolution and are fit with splines to give N_e at the desired heights. For the results at 180 km, the ion composition model correction is applied to the data. However for the $F2$ region results no correction is applied to the data, as the standard ion composition profile which gives nearly 100% O^+ is deemed adequate at these heights.

The nine-position experiment and analysis technique has been described in detail previously [*Buonsanto and Holt*, 1995]. The data analysis method is similar to that used with Arecibo data by *Burnside et al.* [1987]. In brief, we use data collected with both the fixed zenith antenna and the steerable antenna. The latter is pointed at an elevation angle of 45° and is rotated counterclockwise through eight different positions, typically starting at geographic southeast and going through east, northeast, north, northwest, west, southwest, and south, and then clockwise back to southeast. By including both the counterclockwise scan and the succeeding clockwise scan in the analysis, we minimize effects of temporal gradients on the derived velocity field. While a 20–25 min cycle time is typical, we often combine data from two cycles to give better results. The data with 300-μs pulse length are used, and binned over 80 km in altitude about the desired height. From a least squares fit to the data in the nine positions, we are able to estimate the three components of the ion drift vector and their gradients above the station. We also estimate temporal and spatial gradients in N_e, T_e, and T_i.

Table 2. Solar-Geophysical Conditions for Days Included in the Study

Dates	$F_{10.7}$	Ap
Aug. 13, 1980	188.4	6
Jan. 15, 1985	74.9	9
Nov. 10, 1988	150.7	14
Jan. 14, 1990	171.5	8
Sept. 10–12, 1991	184.6, 177.5, 183.1	37, 22, 8
Feb. 5–6, 1992	246.3, 238.6	7, 7
Feb. 29 to March 2, 1992	217.8, 200.4, 181.4	44, 16, 12

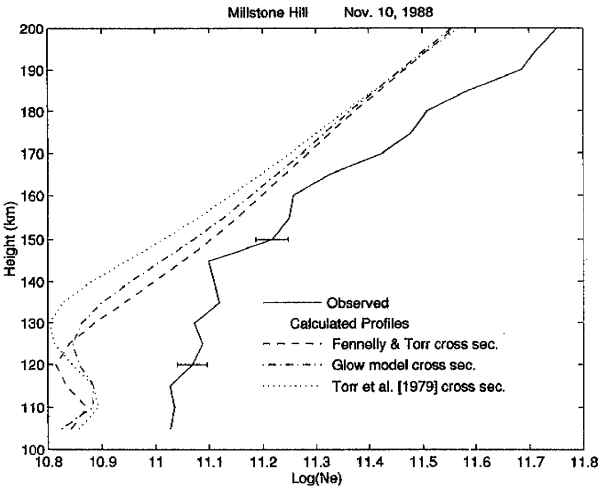

Figure 2. Electron density profiles at Millstone Hill for 1517 UT (1047 LST) on November 10, 1988. The observed profile is shown together with profiles calculated using the Millstone Hill ionospheric model and three different cross section sets. The EUV fluxes input to the model were obtained from sounding rocket measurements on that day.

4. Model/Data Comparisons

In this section we present results of our comparison between Millstone Hill data and model results for the different cross-section sets and EUV flux models. Results are given separately for daytime E-$F1$ region profiles (100–200 km), diurnal variations at a fixed height of 180 km, and the $F2$ region. Table 2 gives the daily $F10.7$ and geomagnetic index Ap for each of the days included in this study.

4.1. E-F1 Region Electron Density Profiles

Figure 2 shows the Millstone Hill N_e profile for 1517 UT (1047 local apparent solar time, LST) on November 10, 1988, together with results from the Millstone Hill model for the three different cross section sets described in section 2.3 above. The EUV fluxes input to the model were measured by a sounding rocket experiment on that day. The instrument and measurements have been described by *Woods and Rottman* [1990]. *Buonsanto et al.* [1992] describe how these solar flux data were bin–averaged into wavelength bins required by the ionospheric model. For this simulation, *pe/pi* ratios were obtained from earlier simulations [*Buonsanto et al.*, 1992] carried out using the GLOW model. The model results for the GLOW model and *Torr et al.* [1979] cross-section sets are very similar to those reported by *Buonsanto et al.* [1992], illustrating that the updates made to the Millstone Hill ionospheric model have little effect on the daytime E-$F1$ region results. The differences between model results for the three different cross section sets are generally much smaller than the differences with the data. The low densities at 130 km resulting from the *Torr et al.* [1979] cross-section set are largely due to the large photoabsorption by O at the short wavelengths. Differences between results for the GLOW and *Fennelly and Torr* [1992] cross sections are largely due to the large O_2 photoionization and photoabsorption cross sections at 977 Å given by

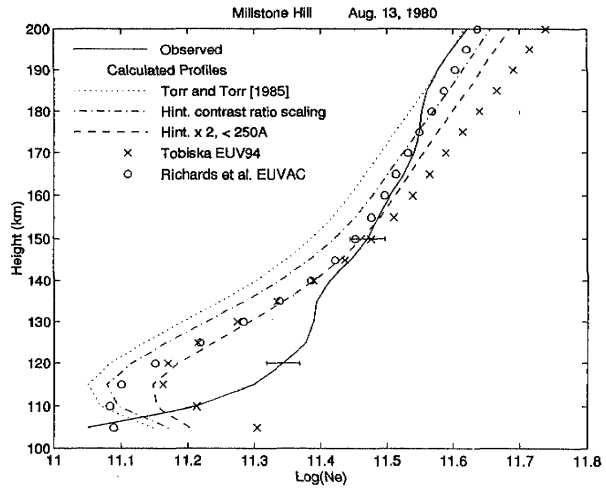

Figure 3. Electron density profiles at Millstone Hill for 1646 UT (1155 LST) on August 13, 1980. The observed profile is shown together with profiles calculated using the Millstone Hill ionospheric model and five different EUV flux models (see text). For all these model simulations, cross sections based on [*Fennelly and Torr*, 1992] were used. The *pe/pi* ratios were obtained from the GLOW model.

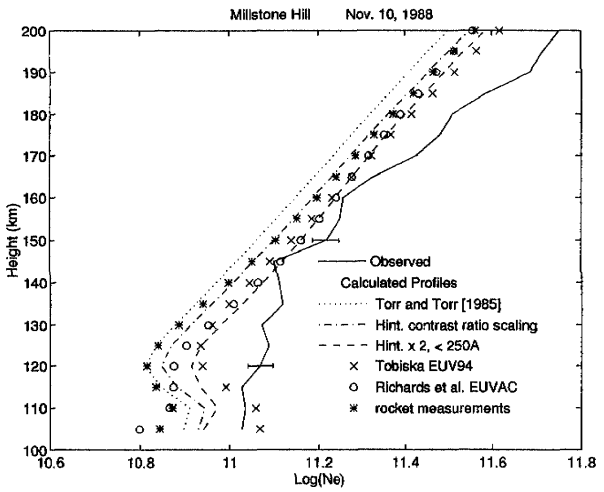

Figure 5. Same as Figure 3, except for 1517 UT (1047 LST) on November 10, 1988, and one additional profile is shown which was obtained using the EUV fluxes from sounding rocket measurements [*Woods and Rottman*, 1990] on that day input to the model.

Fennelly and Torr [1992]. This results in a larger density with the Fennelly and Torr cross sections above 125 km and a lower electron density below 125 km compared to GLOW, and an *E-F*1 valley minimum which is 5 km lower with the Fennelly and Torr cross sections. While this lower *E-F*1 valley minimum seems more consistent with the data, the data do not show a very clear valley minimum. As pointed out by *Buonsanto et al.* [1992], the *E-F*1 valley is a consistent feature in the model results, but only a transient feature in the data.

Figures 3–6 give results from the Millstone Hill model for five different EUV flux models for August 13, 1980, January 15, 1985, Nov. 10, 1988, and Jan. 14, 1990. For all these model simulations, the cross section set based on [*Fennelly and Torr*, 1992] was used. The *pe/pi* ratios were obtained from the GLOW model. The dotted lines give results using linear interpolation between the [*Torr and Torr*, 1985] solar fluxes, using *F*10.7. The dotted-dashed lines give results from the two-class contrast ratio, *F*10.7 association method of [*Hinteregger*, 1981]. The dashed lines give results from using the Hinteregger fluxes, but with values below 250 Å doubled. The crosses give results from using the EUV94X model [*Tobiska*, 1993b, 1994]. The circles give results from the EUVAC model [*Richards et al.*, 1994]. Finally, for November 10, 1988, the asterisks give results from using the EUV rocket measurements on that day [*Woods and Rottman*, 1990].

Near the *E* region peak, the EUV94X fluxes produce the largest electron densities, in better agreement with the data. However, the *E-F*1 valley produced by the EUV94X model seems to be unrealistically deep. The large *E* region peak densities produced by EUV94X result from a high rate of O_2 photoionization due primarily to a large Lyman β flux. The much larger fluxes in the 30–50 Å

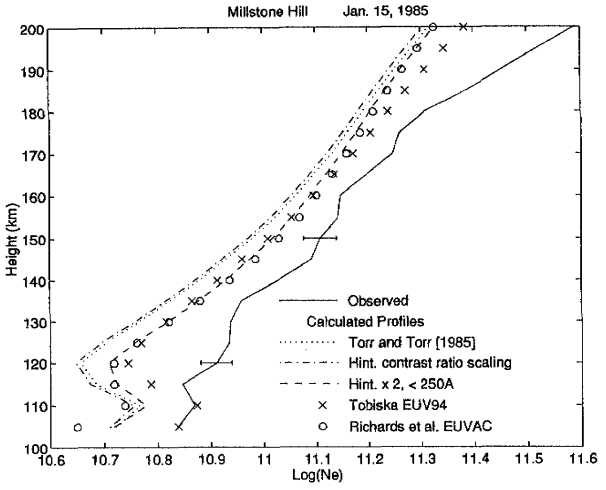

Figure 4. Same as Figure 3, except for 1813 UT (1318 LST) on January 15, 1985.

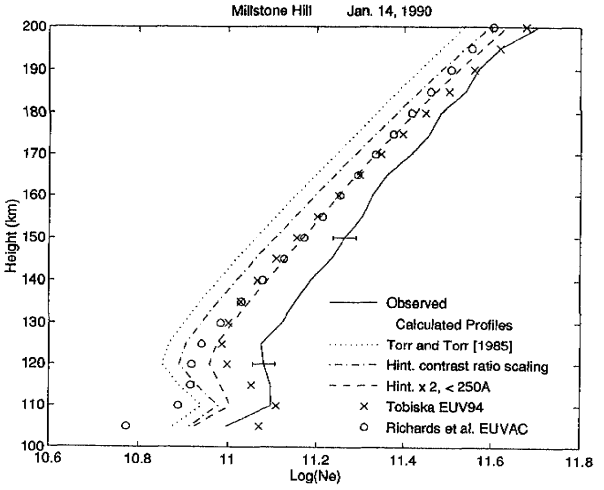

Figure 6. Same as Figure 3, except for 1557 UT (1103 LST) on January 14, 1990.

bin in the EUV94X model also contribute, but their effect is small. In contrast to EUV94X, the EUVAC fluxes produce very low electron densities at the lowest heights, although the shape of the model profile is in reasonable agreement with the data, except for August 13, 1980, when the observations show a large increase in N_e with increasing height through the E region. Above the E-F1 valley there is a level near 140 km where the EUVAC model produces larger electron densities than EUV94X. This results primarily from a larger N_2 photoionization rate. The N_2^+ ions react with atomic oxygen to produce longer lived NO^+ ions. The larger N_2 photoionization rate is due to the larger fluxes in EUVAC in the 50–250 Å range. Above ≈ 160 km, EUV94X produces the largest electron densities. This is due to the combined effects of the larger fluxes at wavelengths greater than 300 Å, primarily on the rate of photoionization of atomic oxygen. In general, the fluxes obtained by linear interpolation between the [*Torr and Torr*, 1985] values and the fluxes from the [*Hinteregger*, 1981] contrast ratio model underestimate the data, except for high altitudes in the summer case. When the Hinteregger fluxes are multiplied by 2 for wavelengths shortward of 250 Å, the calculated electron density profiles look qualitatively similar to those obtained from the EUVAC model, except that the densities at the lowest heights are larger, in better agreement with the N_e data, but not in better agreement with results from the rocket measurements on November 10, 1988 (asterisks in Figure 5).

Figure 5 shows that even when EUV measurements on the same day [*Woods and Rottman*, 1990] are input to the model, the calculated electron densities underestimate the data at all heights. Figure 7 shows the ion concentrations output by the model on this day. Below 140 km, the O_2^+ density is larger than the NO^+ density, although numerous rocket measurements [*Keneshea et al.*, 1970; *Danilov and Semenov*, 1978; *Danilov and Smirnova*, 1993] show a larger NO^+ density. This low NO^+/O_2^+ model density ratio is also a feature of the FLIP model (P. G. Richards, personal communication, 1994). This ratio depends partly on the neutral NO density, since the reaction of O_2^+ with NO is a major source for NO^+. The parameterization of NO density in the Millstone Hill model [*Buonsanto et al.*, 1992] is based on tables provided by *Barth* [1990], which summarize data from the polar-orbiting Solar Mesosphere Explorer satellite. While a larger NO density would increase the NO^+/O_2^+ model density ratio, it would also result in a smaller N_e, since NO^+ recombines more rapidly than O_2^+. This suggests that there is something very important missing in our understanding of this altitude range. An increase in the production rate of NO^+, perhaps from an additional source, or a decrease in its loss rate would be needed to increase the NO^+/O_2^+ model density ratio and at the same time increase the model N_e to values more consistent with the measurements.

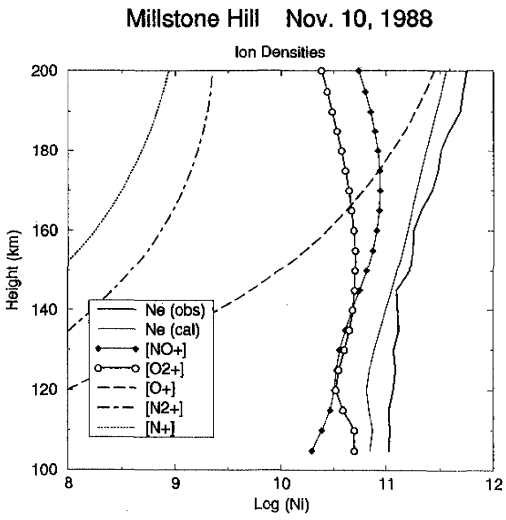

Figure 7. Ion density profiles calculated for 1517 UT (1047 LST) on November 10, 1988, using the rocket measurements as input to the Millstone Hill ionospheric model. Cross sections based on [*Fennelly and Torr*, 1992] and *pe/pi* ratios obtained from the GLOW model were used.

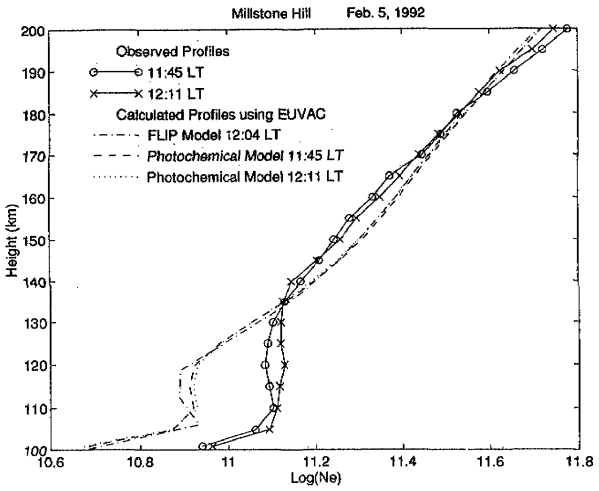

Figure 8. Electron density profiles at Millstone Hill near noon on February 5, 1992. Two incoherent scatter profiles are shown, together with results from both the Millstone Hill ionospheric model and the FLIP model. For the simulations from both ionospheric models the EUVAC solar flux model was used.

A greatly enhanced 1–18 Å X-ray flux, such as during a solar flare, could also increase the electron density as well as the NO^+/O_2^+ ratio. These high-energy photons produce high-energy photoelectrons and Auger electrons which produce multiple ionization (up to a few hundred electrons); and an increased production of N_2^+ results in larger NO and NO^+ densities. R. Link (personal communication, 1995) has recently modeled these processes in detail. For the profiles from the recent solar maximum included in this paper, the GOES 7 1–8 Å X-ray fluxes are well below the level needed to result in significant ionization in Link's model above 100 km. For solar minimum the effects of these X rays are generally quite negligible. We conclude that inclusion of photons with wavelengths below 18 Å in the models would not produce the required increase in electron density and the NO^+/O_2^+ ratio.

Figure 8 shows two incoherent scatter N_e profiles measured at Millstone Hill on February 5, 1992, together with results from both the Millstone Hill ionospheric model and the FLIP model. For the simulations from both ionospheric models the EUVAC solar flux model was used. The photoionization and photoabsorption cross sections for the simulations are also the same, being based on the tabulations of *Fennelly and Torr* [1992], except that as described in section 2.3, the photoionization cross sections for $O^+(^4P)$ and $O^+(^2P^*)$ have been modified in the Millstone Hill model based on results by *Bell and Stafford* [1992]. For the Millstone Hill model, *pe/pi* ratios are obtained from the formulae of [*Richards and Torr*, 1988]. However, for the FLIP model, *pe/pi* ratios are obtained from

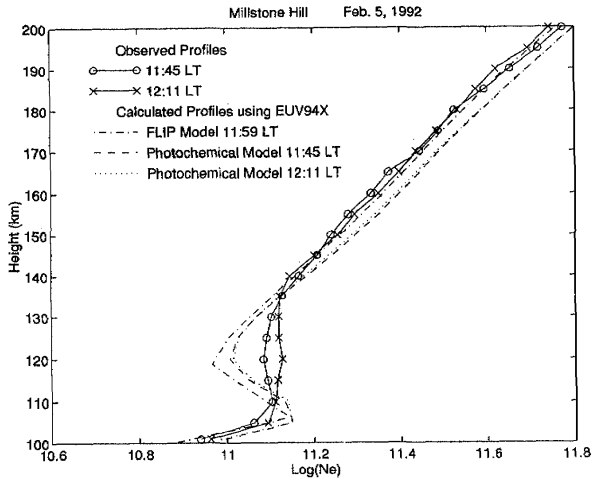

Figure 9. Same as Figure 8, except that the EUV94X solar flux model was used in both the FLIP model and the Millstone Hill ionospheric model simulations.

detailed calculations of photoelectron fluxes. The results from the two ionospheric models are in close agreement although no adjustments were made to either model. This should be expected since the inputs to the two models are nearly the same, but it is encouraging since the results come from very complex calculations carried out by two completely independent ionospheric models. While the model results are in reasonable agreement with the data above 130 km, below this level the model results underestimate the data. As discussed earlier, a larger NO^+ density would be needed to resolve this problem.

Figure 9 shows results of additional simulations carried out by the two ionospheric models, but this time using the EUV94X solar flux model. The other model inputs, as well as the measurements shown are the same as those for Figure 8. As discussed earlier, when the EUV94X model is used, we get a larger *E* region peak density in better agreement with the data, but the *E-F1* valley appears to be too deep compared with the measurements. This time the electron densities output from the FLIP model are a little smaller and in better agreement with the data between 140 and 200 km compared to the Millstone Hill ionospheric model. As discussed earlier the fluxes shortward of 250 Å are very important in this altitude region. The EUV94X model has reduced fluxes in the 50–250 Å range compared to EUVAC, so when EUV94X is used the FLIP model gives significantly smaller photoelectron fluxes, as they depend largely on EUV fluxes at these short wavelengths. The smaller photoelectron fluxes give less production of ionization by secondary photoelectron impact. By contrast, the Millstone Hill model gives the same *pe/pi* ratios when either EUVAC or EUV94X is used. This is because the Millstone Hill model uses the analytical formulae for *pe/pi* from [*Richards and Torr*, 1988], which only depend on the optical depth at 225Å and 977Å. So while the simple *pe/pi* formulae of Richards and Torr are useful and give generally good results, there is a large uncertainty due to the poorly known shape of the solar EUV flux spectrum [*Richards and Torr*, 1988]. Accurate comparison of production rates from different spectra requires a full photoelectron flux solution.

4.2. Diurnal Variations of Electron Density at 180 km

Figure 10 shows the diurnal variation of electron density at a fixed height of 180 km from both the Millstone Hill radar measurements and the Millstone Hill ionospheric model for September 10–12, 1991 and February 29 to March 2, 1992. The solid lines show the observations. Model results are shown for three different EUV flux models. The dotted lines give results using linear interpolation between the [*Torr and Torr*, 1985] solar fluxes, using *F*10.7, the dashed lines give results from using the EUVAC model [*Richards et al.*, 1994], and the dot-dashed lines give results from using the EUV94X model [*Tobiska*, 1993b, 1994]. The photoionization and photoabsorption cross sections for the simulations are our third set based on the tabulations of *Fennelly and Torr* [1992], as described in section 2.3. The *pe/pi* ratios are obtained from the formulae of *Richards and Torr* [1988].

The nighttime data are not very reliable, due to the low signal-to-noise ratio, and the agreement with the model results is not as good as during the day. As seen in Table 2, both of these intervals were geomagnetically disturbed, so the agreement between the model and the data appears quite satisfactory considering the uncertainties in the MSIS-86 composition. EUV94X produces the largest electron densities. This is due to the combined effects of the larger fluxes at wavelengths greater than 300 Å, primarily on the rate of photoionization of atomic oxygen. As discussed above, the larger EUV fluxes in the 50–250Å range in the EUVAC model compared to EUV94X would result in relatively greater ionization by secondary photoelectron impact when using EUVAC. This effect would have the tendency to bring the EUVAC and EUV94X curves into closer agreement than shown in this figure.

4.3. Electron and Ion Temperature

Figure 11 shows observed and FLIP model electron and ion temperature profiles from 100 km up into the topside of the *F*2 region for the same times on February 5, 1992 as in Figures 8 and 9. The

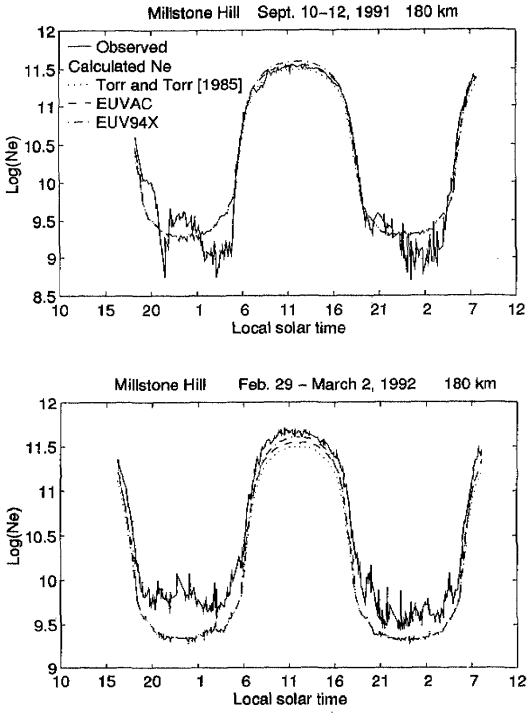

Figure 10. Electron density versus local solar time at a fixed height of 180 km for (top) September 10–12, 1991, and (bottom) February 29 to March 2, 1992. The Millstone Hill radar measurements are shown, together with simulations from the Millstone Hill ionospheric model for three different EUV flux models.

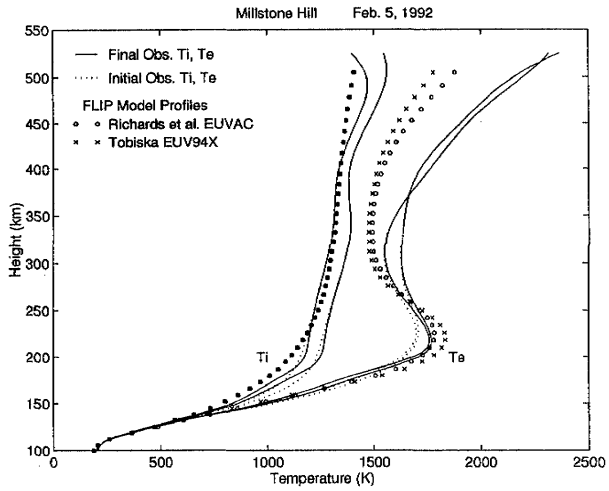

Figure 11. Observed and FLIP model electron and ion temperature profiles from 100 km up into the topside of the $F2$ region for the same times on February 5, 1992, as in Figures 8 and 9. For details see text.

dotted lines show initial observed T_e and T_i profiles, i.e., profiles determined from routine analysis of incoherent scatter data using the standard ion composition profile with 50% O^+ at 180 km. The solid lines show final observed T_e and T_i profiles, i.e., observed profiles which have been corrected using the factors of *Waldteufel* [1971] and the ion composition given by the Millstone Hill model for these times. FLIP model profiles are shown for both the EUVAC and EUV94X model solar fluxes.

The observed profiles which have been corrected by using the Millstone Hill model ion composition are in better agreement with the FLIP model results than the uncorrected data. This indicates the usefulness of the factors of *Waldteufel* [1971], and shows that a two-step process is feasible in which incoherent scatter temperature profiles are first obtained from routine analysis procedures and later corrected using a more sophisticated ion composition model. The agreement between the FLIP model and the data is quite good, except for T_e above the $F2$ peak. The discrepancy between the measured and modeled T_e above 300 km is due to the heat flow into the ionosphere from the plasmasphere. The processes that heat the plasmaspheric electrons are poorly characterized at present. The minimum in T_e near 300 km is due to an increased cooling rate due to the larger ion density. The FLIP model T_i is insensitive to the choice of EUV flux model. However, the FLIP model T_e is a little larger near 150 km when the EUVAC model is used because of the larger fluxes shortward of 250Å which are important near this altitude. In the F region T_e is larger when the EUV94X model is used because of the larger EUV fluxes at longer wavelengths.

4.4. F2 region

4.4.1. FLIP model results. Figures 8 and 9 showed FLIP model profiles compared to radar data for near local noon on February 5, 1992 for the altitude region 100–200 km only. Figure 12 shows the same profiles extended to heights above the $F2$ peak. In the F region the agreement between the FLIP model and the data is excellent at all heights when the EUVAC model fluxes are used. When the fluxes from EUV94X are input to the FLIP model, the photoionization rate at the $F2$ peak increases by 47%; however, production by secondary photoelectron impact decreases by 29% because the photoelectron fluxes are decreased by the smaller EUV fluxes shortward of 250Å. The overall result is that the higher photoionization rate using EUV94X compared to EUVAC is partially compensated by the smaller rate of production by photoelectron impact, such that the FLIP model $F2$ peak electron densities are 23% higher when EUV94X is used. A discrepancy of this size between the data and the model may still be regarded as acceptable, considering the uncertainties expected in any EUV flux model, as well as uncertainties in cross sections and reaction rates and a 20–25% uncertainty in the MSIS-86 atomic oxygen density [*Hedin*, 1987]. Additional simulations with the FLIP model for a solar minimum case (not shown) showed that the $F2$ peak electron density was only 7% higher when EUV94X was used, compared to EUVAC, although the photoionization frequency was 25% larger.

4.4.2. Semiempirical model results. Figures 13, 14, and 15 show results from the Millstone Hill semiempirical model for the $F2$ region for three nine-position experiments during the last solar cycle maximum period. The electron density at a fixed height is shown in the top panel of each figure. Solid lines show the incoherent scatter radar data, while the other curves give model results for the EUVAC and EUV94X solar flux models and for linear interpolation with $F10.7$ between the EUV fluxes of [*Torr and Torr*, 1985]. The photoionization and photoabsorption cross sections for these simulations are our third set based on the tabulations of *Fennelly and Torr* [1992], as described in section 2.3. The *pe/pi* ratios are obtained from the formulae of *Richards and Torr* [1988].The semiempirical model results were obtained by solving equation (3), as described in section 2.1.2 above. The $O^+(^4S)$ recombination rate β is shown in the bottom panel of each figure. Solid lines show β calculated from the MSIS-86 model using equation (5). The other curves show β derived from the incoherent scatter data and the modeled production rates using the three EUV flux models and equation (4).

The best overall agreement between the ionospheric model and the radar data is on February 5–6, 1992 (Figure 14). This is not at all surprising, since this was a geomagnetically much quieter interval than the other two periods (Table 2), so that the MSIS-86 model is expected to be more accurate. The ≈ 50 min (or worse) temporal resolution of the model results is insufficient to follow some of the more rapid variations in the data. Model results are missing whenever radar data were missing from 1 or more of the nine pointing

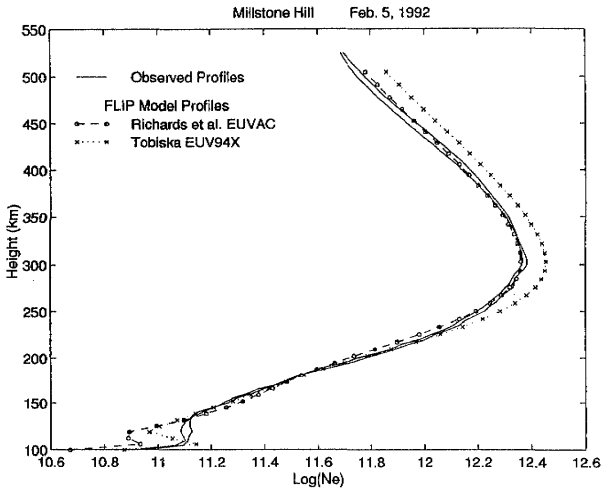

Figure 12. The observed and FLIP model electron density profiles of Figures 8 and 9 extended upward into the topside of the $F2$ region.

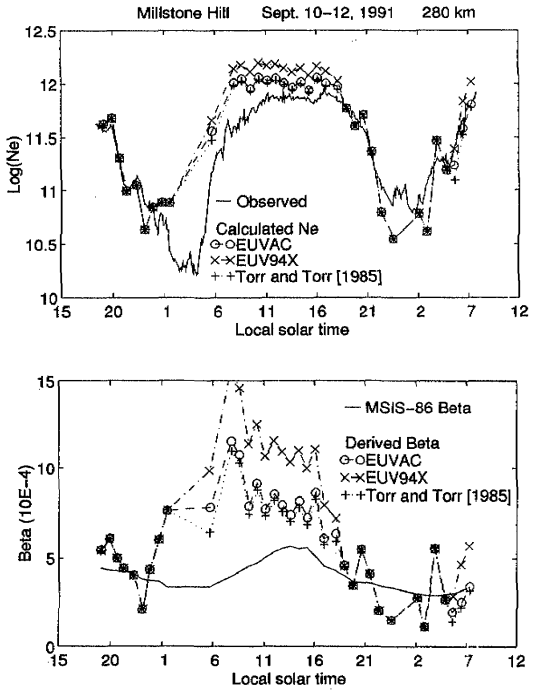

Figure 13. Observations and results of the Millstone Hill semiempirical ionospheric model for a fixed height of 280 km on September 10–12, 1991. (top) Millstone Hill radar electron density measurements, together with calculated electron density for three different EUV flux models. (bottom) The $O^+(^4S)$ recombination rate β calculated from the MSIS-86 model using equation (5), and derived from the incoherent scatter data and the modeled production rates using the three EUV flux models and equation (4).

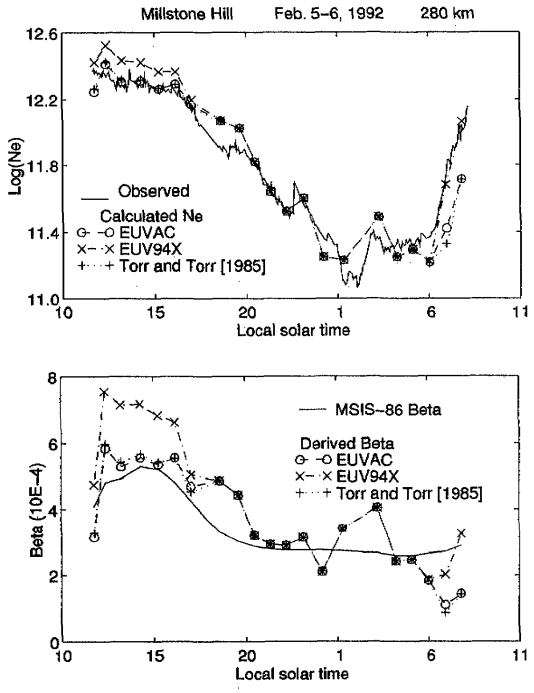

Figure 14. Same as Figure 13, except for February 5–6, 1992.

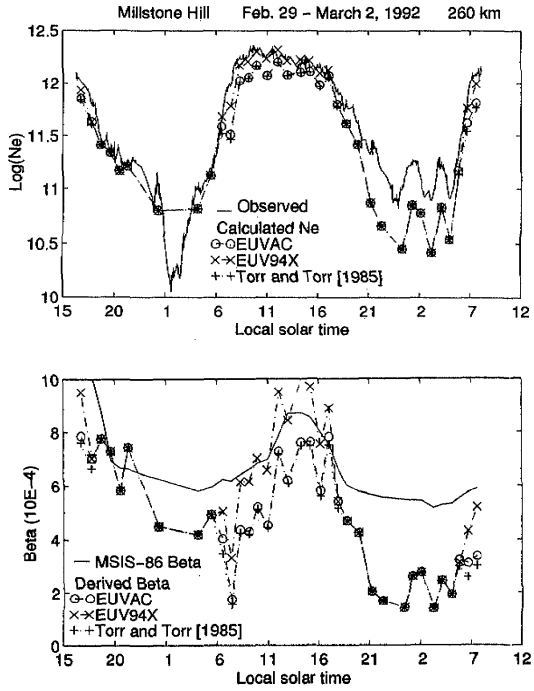

Figure 15. Same as Figure 13, except for a fixed height of 260 km on February 29 to March 2, 1992.

positions, so that it was not possible to estimate gradients in N_e and in the components of the ion velocity vector. However, the semiempirical model does reproduce the wave-like feature seen in the N_e data on March 2, 1992. The daytime model results illustrate the effects of using the different EUV flux models. As expected, the model N_e is largest when EUV94X is used. However, as discussed above, the semiempirical model uses the same *pe/pi* ratios for all the EUV flux models, so the differences between the EUVAC and EUV94X model results would be smaller if the differing shapes of the EUV model spectra on the *pe/pi* ratios were taken into account. The results from using the *Torr and Torr* [1985] EUV fluxes are very similar to the EUVAC results for all three of these solar maximum data sets. For the recombination rates, the MSIS-86 results are in reasonable agreement with the derived β for the quiet interval February 5–6, 1992 (bottom panel of Figure 14). The MSIS-86 β are too small during the daytime compared to the derived β for the disturbed interval September 10–12, 1991 (Figure 13), and too large at night for the disturbed interval February 29 to March 2, 1992 (Figure 15). In general, the derived β show a larger diurnal variation than the MSIS-86 results.

5. Conclusions

In this work we have described the Millstone Hill semiempirical ionospheric model, which has been developed from the photochemistry of [*Buonsanto et al.*, 1992]. This model gives very similar results to the FLIP model for the *E* and *F*1 regions. For the *F*2 region, the Millstone model uses estimates of the motion term in the electron density continuity equation derived from nine-position radar data.

Results from the Millstone model and the FLIP model underestimate the measured N_e in the *E* region, except that the EUV94X solar flux model produces reasonable agreement with the radar data

at the E region peak because of a large Lyman β (1026 Å) flux, but produces an unrealistically deep E-$F1$ valley. Both the Millstone model and the FLIP model give O_2^+ densities larger than NO^+ densities in the E region, though numerous rocket and satellite measurements give a larger NO^+ density. This suggests that our understanding of the NO^+ chemistry may be incomplete. An additional source or faster production rate for NO^+, or a slower loss rate would increase the calculated N_e to agree better with the radar data, and also remove the discrepancy with rocket and satellite ion composition measurements.

The EUV94X model has larger fluxes compared to the EUVAC model over the entire 300–1050 Å range, apart from some individual spectral lines. The EUVAC model has larger fluxes over the 50–250 Å interval. The result is a larger photoionization rate with EUV94X compared to EUVAC at all levels of the ionosphere, except for a height interval near 140 km, where the 50–250 Å fluxes are most important. However, the larger photoionization rates from EUV94X are partially compensated for by a smaller rate of ionization due to secondary photoelectron impact, because the photoelectron fluxes depend strongly on the incident solar flux shortward of ≈ 300 Å. The differences between model results for the three different cross section sets are generally much smaller than the differences with the data.

Rates of recombination of $O^+(^4S)$ β obtained from using the MSIS-86 model agree reasonably well with β derived from the model production rates and the radar measurements for the quiet interval February 5–6, 1992. Significant discrepancies were found for two more disturbed intervals, however. This illustrates that the MSIS-86 model should be used with great caution during disturbed periods, when actual measurements of neutral composition are highly desirable.

Acknowledgments. We are grateful to R. Link of Southwest Research Institute for useful discussions and to A. E. Hedin of the Goddard Space Flight Center for providing the MSIS-86 model. Millstone Hill radar data were acquired and analyzed under the support of National Science Foundation cooperative agreements ATM-91-02445 and ATM-94-08609 to the *Massachusetts Institute of Technology*. *Work by P. G. Richards was supported by NASA grant NAGW996.* W. K. Tobiska gratefully acknowledges the support of Telos Information Systems for his research.

The Editor thanks R. R. Meier and another referee for their assistance in evaluating this paper.

References

Abdou, W. A., D. G. Torr, P. G. Richards, M. R. Torr, and E. L. Breig, Results of a comprehensive study of the photochemistry of N_2^+ in the ionosphere, *J. Geophys. Res.*, *89*, 9069–9079, 1984.

Barth, C. A., Reference models for thermospheric NO, *Adv. Space Res.*, *10*(6), 103–115, 1990.

Bell, K. L., and R. P. Stafford, Photoionization cross-sections for atomic oxygen, *Planet. Space Sci.*, *40*, 1419–1424, 1992.

Buonsanto, M. J., Comparison of incoherent scatter observations of electron density, and electron and ion temperature at Millstone Hill with the International Reference Ionosphere, *J. Atmos. Terr. Phys.*, *51*, 441–468, 1989.

Buonsanto, M. J., A study of the daytime *E-F1* region ionosphere at midlatitudes, *J. Geophys. Res.*, *95*, 7735–7747, 1990.

Buonsanto, M. J., and J. M. Holt, Measurements of gradients in ionospheric parameters with a new nine position experiment at Millstone Hill, *J. Atmos. Terr. Phys., in press, 1995.*

Buonsanto, M. J., S. C. Solomon, and W. K. Tobiska, Comparison of measured and modeled solar EUV flux and its effect on the *E-F1* region ionosphere, *J. Geophys. Res.*, *97*, 10,513–10,524, 1992.

Burnside, R. G., J. C. G. Walker, and M. P. Sulzer, Kinematic properties of the F region ion velocity field inferred from incoherent scatter radar measurements at Arecibo, *J. Geophys. Res.*, *92*, 3345–3355, 1987.

Chang, T., D. G. Torr, P. G. Richards, and S. C. Solomon, Reevaluation of the $O^+(^2P)$ reaction rate coefficients from Atmosphere Explorer C observations, *J. Geophys. Res.*, *98*, 15,589–15,597, 1993.

Conway, R. R., Photoabsorption and photoionization cross sections of O, O_2, and N_2 for photoelectron production calculations: A compilation of recent laboratory measurements, *NRL Mem. Rep. 6155*, Nav. Res. Lab., Washington, D. C., 1988.

Danilov, A. D., and V. K. Semenov, Relative ion composition model at midlatitudes, *J. Atmos. Terr. Phys.*, *40*, 1093–1102, 1978.

Danilov, A. D., and N. V. Smirnova, Ionic composition and photochemistry of the lower thermosphere, 2, Ion composition of the D and E regions, *Geomagn. Aeron.*, Engl. Transl., *33*, 94–104, 1993.

Evans, J. V., Theory and practice of ionosphere study by Thomson scatter radar, *Proc. IEEE*, *57*, 496–530, 1969.

Fehsenfeld, F. C., The reaction of O_2^+ with atomic nitrogen and $NO^+ \cdot H_2O$ and NO_2^+ with atomic oxygen, *Planet. Space Sci.*, *25*, 195–196, 1977.

Fennelly, J. A., and D. G. Torr, Photoionization and photoabsorption cross sections of O, N_2, O_2, and N for aeronomic calculations, *At. Data Nucl. Data Tables*, *51*, 321–363, 1992.

Hedin, A. E., MSIS-86 thermospheric model, *J. Geophys. Res.*, *92*, 4649–4662, 1987.

Henry, R. J. W., P. G. Burke, and A. L. Sinfailam, Scattering of electrons by C, N, O, N^+, O^+, and O^{++}, *Phys. Rev.*, *178*, 218–224, 1969.

Heroux, L., and H. E. Hinteregger, Aeronomical reference spectrum for solar UV below 2000 Å, *J. Geophys. Res.*, *83*, 5305–5308, 1978.

Hinteregger, H. E., Representations of solar EUV fluxes for aeronomical applications, *Adv. Space Res.*, *1*, 39–52, 1981.

Hinteregger, H. E., K. Fukui, and B. R. Gilson, Observational, reference and model data on solar EUV, from measurements on AE-E, *Geophys. Res. Lett.*, *8*, 1147–1150, 1981.

Johnsen, R., and M. A. Biondi, Laboratory measurements of the $O^+(^2D)$ + N_2 and $O^+(^2D)$ + O_2 reaction rate coefficients and their ionospheric implications, *Geophys. Res. Lett.*, *7*, 401–403, 1980.

Keneshea, T. J., R. S. Narcisi, and W. Swider Jr., Diurnal model of the E region, *J. Geophys. Res.*, *75*, 845–854, 1970.

Kirby, K., E. R. Constantinides, S. Babeu, M. Oppenheimer, and G. A. Victor, Photoionization and photoabsorption cross sections of thermospheric species: He, O, N_2, and O_2, *At. Data Nucl. Data Tables*, *23*, 63–81, 1979.

Langford, A. O., V. M. Bierbaum, and S. R. Leone, Auroral implications of recent measurement of $O(^1S)$ and $O(^1D)$ formation in the reaction of N^+ with O_2, *Planet. Space Sci.*, *33*, 1225–1228, 1985.

Lean, J., A comparison of models of the Sun's extreme ultraviolet irradiance variations, *J. Geophys. Res.*, *95*, 11,933–11,944, 1990.

Lilensten, J., W. Kofman, J. Wisemberg, E. S. Oran, and C. R. Devore, Ionization efficiency due to primary and secondary photoelectrons: A numerical model, *Ann. Geophys.*, *7*, 83–90, 1989.

Lindinger, W., F. C. Fehsenfeld, A. L. Schmeltekopf, and E. E. Ferguson, Temperature dependence of some ionospheric ion-neutral reactions from 300°K–900°K, *J. Geophys. Res.*, *79*, 4753–4756, 1974.

Link, R., Dayside magnetospheric cleft auroral processes, Ph.D. thesis, 489 pp., York Univ., Toronto, 1982.

McFarland, M., D. L. Albritton, F. C. Fehsenfeld, E. E. Ferguson, and A. L. Schmeltekopf, Energy dependence and branching ratio of the N_2^+ + O reaction, *J. Geophys. Res.*, *79*, 2925–2926, 1974.

Nagy, A. F., and P. M. Banks, Photoelectron fluxes in the ionosphere, *J. Geophys. Res.*, *75*, 6260–6270, 1970.

Ogawa, H. S., and D. L. Judge, Absolute solar flux measurement shortward of 575Å, *J. Geophys. Res.*, *91*, 7089–7092, 1986.

Rees, M. H., *Physics and Chemistry of the Upper Atmosphere*, 289 pp., Cambridge University Press, New York, 1989.

Richards, P. G., and D. G. Torr, An investigation of the consistency of the ionospheric measurements of the photoelectron flux and solar EUV flux, *J. Geophys. Res.*, *89*, 5625–5635, 1984.

Richards, P. G., and D. G. Torr, Ratios of photoelectron to EUV ionization rates for aeronomic studies, *J. Geophys. Res.*, *93*, 4060–4066, 1988.

Richards, P. G., J. A. Fennelly, and D. G. Torr, EUVAC: A solar EUV flux

model for aeronomic calculations, *J. Geophys. Res.*, *99*, 8981–8992, 1994. (Correction, *J. Geophys. Res.*, *99*, 13,283, 1994.)

Samson, J. A. R., and P. N. Pareek, Absolute photoionization cross sections of atomic oxygen, *Phys. Rev. A*, *31*, 1470–1476, 1985.

Schunk, R. W., and A. F. Nagy, Electron temperatures in the *F* region of the ionosphere: Theory and observations, *Rev. Geophys. Space Phys.*, *16*, 355–399, 1978.

Seaton, M. J., and D. W. Osterbrock, Relative OII intensities in gaseous nebulae, *Astrophys. J.*, *125*, 66–83, 1957.

Solomon, S. C., and V. J. Abreu, The 630 nm dayglow, *J. Geophys. Res.*, *94*, 6817–6824, 1989.

Solomon, S. C., P. B. Hays, and V. J. Abreu, The auroral 6300 Å emission: Observations and modeling, *J. Geophys. Res.*, *93*, 9867–9882, 1988.

St.-Maurice, J.-P., and R. W. Schunk, Diffusion and heat flow equations for the mid-latitude topside ionosphere, *Planet. Space Sci.*, *25*, 907–920, 1977.

St.-Maurice, J.-P., and D. G. Torr, Nonthermal rate coefficients in the ionosphere: The reactions of O^+ with N_2, O_2, and NO, *J. Geophys. Res.*, *83*, 969–977, 1978.

Strobel, D. F., T. R. Young, R. R. Meier, T. P. Coffey, and A. W. Ali, The nighttime ionosphere: *E* region and lower *F* region, *J. Geophys. Res.*, *79*, 3171–3178, 1974.

Strobel, D. F., C. B. Opal, and R. R. Meier, Photoionization rates in the night-time *E*- and *F*-region ionosphere, *Planet. Space Sci.*, *28*, 1027–1033, 1980.

Titheridge, J. E., An approximate form for the Chapman grazing incidence function, *J. Atmos. Terr. Phys.*, *50*, 699–701, 1988.

Tobiska, W. K., Recent solar extreme ultraviolet irradiance observations and modeling: A review, *J. Geophys. Res.*, *98*, 18,879–18,893, 1993a.

Tobiska, W. K., The empirical solar EUV irradiance model EUV94 (abstract), *Eos Trans. AGU*, *74*(43), Fall Meeting suppl., 490, 1993b.

Tobiska, W. K., Modeled soft X-ray solar irradiances, *Solar Phys.*, *152*, 207–215, 1994.

Torr, D. G., The photochemistry of the upper atmosphere, in *The Photochemistry of Atmospheres*, edited by J. S. Levine, pp. 165–278, Academic, San Diego, Calif., 1985.

Torr, D. G., M. R. Torr, J. C. G. Walker, A. O. Nier, L. H. Brace, and H. C. Brinton, Recombination of O_2^+ in the ionosphere, *J. Geophys. Res.*, *81*, 5578–5580, 1976.

Torr, D. G., P. G. Richards, and M. R. Torr, Photochemistry of the ionosphere, in *World Ionosphere Thermosphere Study WITS Handbook*, vol. 1, edited by C. H. Liu and B. Edwards, pp. 1–38, SCOSTEP Secretariat, Urbana, Ill., 1988.

Torr, M. R., and D. G. Torr, Recombination of NO^+ in the mid-latitude trough and the polar ionization hole, *J. Geophys. Res.*, *84*, 4316–4320, 1979.

Torr, M. R., and D. G. Torr, Ionization frequencies for solar cycle 21: Revised, *J. Geophys. Res.*, *90*, 6675–6678, 1985.

Torr, M. R., D. G. Torr, R. A. Ong, and H. E. Hinteregger, Ionization frequencies for major thermospheric constituents as a function of solar cycle 21, *Geophys. Res. Lett.*, *6*, 771–774, 1979.

Torr, M. R., D. G. Torr, P. G. Richards, and S. P. Yung, Mid- and low-latitude model of thermospheric emissions, 1, $O^+(^2P)$ 7320 Å and N_2 (2*P*) 3371 Å, *J. Geophys. Res.*, *95*, 21,147–21,168, 1990.

Tung, Y.-K., Extension of a Millstone Hill ionospheric model, B.Sc. thesis, 41 pp., Mass. Inst. of Tech., Cambridge, May 1993.

Waldteufel, P., Combined incoherent scatter F_1-region observations, *J. Geophys. Res.*, *76*, 6995–6999, 1971.

Walls, F. L., and G. H. Dunn, Measurement of total cross sections for electron recombination with NO^+ and O_2^+ using ion storage techniques, *J. Geophys. Res.*, *79*, 1911–1915, 1974.

Woods, T. N., and G. J. Rottman, Solar EUV irradiance derived from a sounding rocket experiment on November 10, 1988, *J. Geophys. Res.*, *95*, 6227–6236, 1990.

M. J. Buonsanto, Haystack Observatory, Atmospheric Sciences Group, Massachusetts Institute of Technology, Westford, MA 01886. (e-mail: mjb@oceanus.haystack.edu)

J. A. Fennelly, Earth System Science Laboratory, University of Alabama, Huntsville, AL 35899. (e-mail: fennellyj@csparc.uah.edu)

P. G. Richards, Computer Science Department and Center for Space Plasma and Aeronomic Research, University of Alabama, Huntsville, AL 35899. (e-mail: richards@cs.uah.edu)

S. C. Solomon, Laboratory for Atmospheric and Space Physics, University of Colorado, Boulder, CO 80309. (e-mail: solomon@tethys.colorado.edu)

W. K. Tobiska, Telos/Jet Propulsion Laboratory, Pasadena, CA 91109. (e-mail: ktobiska@gllsvc.jpl.nasa.gov)

Y.-K. Tung, Physics Department, University of California, Berkeley, CA 94720. (e-mail: yktung@physics.berkeley.edu)

(Received December 12, 1994; revised February 21, 1995; accepted February 23, 1995.)